Applied Catalysis B: Environmental 205 (2017) 133–147

Contents lists available at ScienceDirect

Applied Catalysis B: Environmental

journal homepage: www.elsevier.com/locate/apcatb

Novel ternary heterojunction photcocatalyst of Ag nanoparticles and g-C_3N_4 nanosheets co-modified $BiVO_4$ for wider spectrum visible-light photocatalytic degradation of refractory pollutant

Fei Chen[a,b], Qi Yang[a,b,*], Yali Wang[a,b], Jianwei Zhao[a,b], Dongbo Wang[a,b,*], Xiaoming Li[a,b], Zhi Guo[a,b], Hou Wang[a,b], Yaocheng Deng[a,b], Chenggang Niu[a,b], Guangming Zeng[a,b]

[a] College of Environmental Science and Engineering, Hunan University, Changsha 410082, PR China
[b] Key Laboratory of Environmental Biology and Pollution Control (Hunan University), Ministry of Education, Changsha 410082, PR China

ARTICLE INFO

Article history:
Received 31 August 2016
Received in revised form 3 November 2016
Accepted 7 December 2016
Available online 8 December 2016

Keywords:
Heterojunction
Ag@g-C_3N_4@$BiVO_4$
Photocatalysis
Synergistic effect
Z-scheme mechanism

ABSTRACT

A novel and highly efficient three-component Ag@g-C_3N_4@$BiVO_4$ heterojunction was successfully synthesized and characterized in terms of structure, porosity, chemical composition and optical properties. The photocatalytic activities of as-prepared samples were evaluated by the photocatalytic decomposition of tetracycline (TC) in the aqueous phase. Compared with single semiconductor $BiVO_4$ and g-C_3N_4, binary composites Ag@$BiVO_4$ and g-C_3N_4@$BiVO_4$, the ternary Ag@g-C_3N_4@$BiVO_4$ heterojunction exhibited the higher photocatalytic activity under wider light spectrum irradiation. Furthermore, we also investigated the effects of initial TC concentrations and coexisting ions were in simulated practical wastewater. The mechanism research showed that matching of band structure between $BiVO_4$ and g-C_3N_4 induced an efficient photogenerated electrons and holes transfer from the CB of $BiVO_4$ and VB of g-C_3N_4, respectively. As a charge transfer center, Ag nanoparticles were well photodeposited onto the surface of $BiVO_4$ and g-C_3N_4 and increased the visible light absorption, even near-infrared via the surface plasmon resonance. The synergy effects between Ag, g-C_3N_4 and $BiVO_4$ with the aid of Z-scheme mechanism were the main reason for improved photocatalytic performance. The trapping experiments and ESR tests confirmed that the $\bullet O_2^-$, h^+ and •OH were main active species in photocatalytic degradation of TC. From the viewpoint of practical application, Ag@g-C_3N_4@$BiVO_4$ ternary structure displayed superior photostability after four times recycle.

© 2016 Elsevier B.V. All rights reserved.

1. Introduction

Heterogeneous photocatalysis using solar energy has been regarded as a promising alternative strategy for environmental protection and remediation, particularly for the removal of hazardous organic compounds from wastewater [1–4]. Thus, exploiting the novel, high-efficient and environment-friendly photocatalysts are urgent and necessary for the long-term development. The constructing photocatalytic systems should possess the following advantages: (I) efficient capability of harvesting visible light; (II) effective visible light converting by electron-hole pair creation and charge separation; (III) better performance to trigger redox reactions for photocatalytic performance enhancement [5,6]. A large number of methods have been developed to decorate photocatalysts for achieving perferable visible light response, including metal or non-metal doping, facet and morphology control, heterojunction built and so forth [7–10]. Among these approaches, construction of a semiconductor heterojunction has aroused great research concern because heterojunction construction facilitated the photocatalytic activity enhancement to a greater extent. According to previous reports [11,12], construction of two photo-reactive semiconductors with suitable electronic structures usually exhibited more superior photoactivity than single photocatalyst. The accelerated charge separation by the internal electric field in the heterojunctions had become the driving force of photocatalytic performance enhancement. The unique band structures including the band gap and energy levels of the conduction band and the valence band should be the predominant reasons [13]. Under the optical band structures conditions, the photo-induced electrons and holes from one semiconductor could efficiently transfer to the coupled semiconductor and facilitate the charge carrier separation, leaving

* Corresponding author.
E-mail addresses: feichen@hnu.edu.cn (F. Chen), yangqi@hnu.edu.cn (Q. Yang), w.dongbo@yahoo.com (D. Wang).

http://dx.doi.org/10.1016/j.apcatb.2016.12.017
0926-3373/© 2016 Elsevier B.V. All rights reserved.

more electrons and holes to anticipate in the photocatalytic process [14,15].

In this work, multi-component heterojunction was taken as the model photocatalytic system based on the following considerations. Recent studies have confirmed that $BiVO_4$ is one of the most promising visible light active photocatalysts. The narrow band gap (about 2.4 eV) and high abundance prompted its significant applications in the fields of organic pollutants degradation under visible light irradiation [16,17]. Nevertheless, there are several inherent drawbacks for single $BiVO_4$, such as its poor visible light harvesting efficiency, high photogenerated charge recombination rate, low quantum yield and poor adsorption capacity, which have severely restricted its practical use [18,19]. As mentioned above, the construction of heterojunction with matched conduction and valence band is advantageous for tuning the electronic structures and moreover photophysical and photochemical properties of $BiVO_4$. The $BiVO_4$-based heterojunctions could extend the visible light absorption range, improve the photo-induced electron-hole pairs separation and interfacial transfer efficiencies and possessed as higher photocatalytic performance. Successful cases such as, g-C_3N_4/$BiVO_4$ [20], Cu_2O/$BiVO_4$ [21], MoS_2/$BiVO_4$ [22], CeO_2/$BiVO_4$ [23], Ag_2O@$BiVO_4$ [24] and so on had been designed in previous researches. Of these, coupling $BiVO_4$ with graphitic g-C_3N_4 is more potential for the advantages including a layered structure, high thermal and chemical stability and negative conduction band (CB, −1.23 eV vs. NHE), which makes its photoinduced CB electrons with strong reducing characteristics [20,25,26]. Furthermore, the well-matched band position of g-C_3N_4 and $BiVO_4$ was presented, indicated by the highly positive valence band (VB) of $BiVO_4$ and the highly negative CB of g-C_3N_4. Through the efficient heterojunction transfer, the corresponding charge carrier lifetime would be significantly prolonged, resulting in an enhanced visible light photocatalytic performance. Thus g-C_3N_4@$BiVO_4$ binary system was taken into investigation in this work.

Recently, most efforts of heterstructured photocatalysis have been devoted on binary heterojunctions. However, the limited region of visible light response and relatively low charge separation efficiency in these binary systems also become the stumbling block [27]. Certainly, the similar problems might also exist in the g-C_3N_4@$BiVO_4$ system. To address these issues, the development of multi-component heterojunction systems is indispensable. These systems possessed two or more visible light responsive components and form a more efficient charge transfer system [28]. Furthermore, the addition of small amount of noble metal nanoparticles (e.g., Au, Ag) to conventional semiconductors can boost the photoelectrochemical properties and offer a new opportunity to overcome the limited photocatalytic efficiency of photocatalysts and imperfect photovoltaic devices [29,30]. Two ascendant aspects could be listed for the introduction of noble metal nanoparticles. On one hand, the strongly visible light absorption and solar energy transferring could induce the efficient photogenerated electron-hole pairs separation and promote the visible-light-driven photoactivity [31]. On the other hand, the charge transfer process between semiconductors could be accelerated with the role of electrons traps by noble metallic nanoparticles, which could further enhance the photocatalytic performance [32,33]. Our group had successfully prepared Ag nanoparticles and RGO co-modified $BiVO_4$ [34] and Ag_3PO_4@$BiVO_4$ [35] photocatalysts and the obtained results had demonstrated that the introduction of metallic Ag played a vital role in the charge separation promotion and photoactivity enhancement. Combining with aforementioned analysis, in order to utilize solar energy to generate electron-hole pairs for boosting photocatalytic activity, it is desirable and meaningful to construct a ternary Ag@g-C_3N_4@$BiVO_4$ heterojunction. To the best of our knowledge, relative reports about ternary $BiVO_4$-based heterojunctions are quietly scarce.

In present work, metallic Ag and g-C_3N_4 nanosheets co-modified $BiVO_4$ photocatalyst was prepared and applied in the degradation of tetracycline (TC). The g-C_3N_4@$BiVO_4$ composite was firstly fabricated by a wet-impregnation procedure, followed by a typical photo-deposition method to homogenously deposit Ag nanoparticles on the surface of $BiVO_4$ and g-C_3N_4. The chemical compositions, morphology structures, photocatalytic activities and photostability were fully characterized and discussed. Taking the practical application into consideration, the effects of initial TC concentration and coexisting ions were also investigated. Moreover, the coupling effects of metallic Ag and g-C_3N_4 on $BiVO_4$ were systematically studied in an attempt to explore the possible mechanisms for the significantly improved photocatalytic activity towards the decomposition of refractory pollutants. It is anticipated that our work could be helpful for the fabrication of more novel ternary composite photocatalysts.

2. Experimental section

2.1. Materials

Bismuth nitrate pentahydrate ($Bi(NO_3)_3{\cdot}5H_2O$), ammonium metavanadate (NH_4VO_3), silver nitrate ($AgNO_3$), aqueous ammonia ($NH_3{\cdot}H_2O$), glacial acetic acid (CH_3COOH), melamine ($C_3N_3(NH_2)_3$), methanol (CH_3OH), ethanol (CH_3CH_2OH), nano titanium dioxide (TiO_2) and tetracycline (TC) were obtained commercially from Ainopharm Chemical Reagent Co., Ltd. All the reagents and materials were of analytical grade and used as received without additional purification or treatment. De-ionized water (18.25 MΩ cm) was used in the whole experiment.

2.2. Preparation of g-C_3N_4

The g-C_3N_4 lamellar structure was prepared using modified version of previously reported two-step thermal treatment method [36]. In the first thermal step, 10 g of melamine was placed into a ceramic crucible with a cover and then loaded into the central region of a muffle furnace. The crucible was firstly heated to 500 °C with a heating rate of 2 °C/min and maintained at 500 °C for 2 h, and followed by heating 520 °C for another 2 h at the same heating rate. After cooling to ambient temperature, the obtained yellow agglomerate (bulk g-C_3N_4) was ground into powder. In the second thermal step (thermal exploitation process), 2 g of the above-obtained bulk g-C_3N_4 was put into an open ceramic crucible and heated at 520 °C at a heating rate of 2 °C/min and kept at 520 °C for 4 h, and then allowed to cool to room temperature naturally. The g-C_3N_4 lamellar structure was achieved in powder form for future use.

2.3. Preparation of $BiVO_4$ nanorods

The $BiVO_4$ nanorods were fabricated via a facile hydrothermal method. In a typical synthesis, 5 mmol of $Bi(NO_3)_3{\cdot}5H_2O$ was completely dissolved in 10 mL of glacial acetic acid with constant stirring. Simultaneously, 5 mmol of NH_4VO_3 was dissolved in 60 mL of hot water (about 80 °C). Subsequently, the latter solution was dropwise added into the former one with 20 min ultrasonic treatment and 30 min room stirring, resulting in the formation of yellow precipitate, followed by adjustment of the pH to be 9 by the addition of certain volume of $NH_3{\cdot}H_2O$. The mixture was vigorously stirred for 2 h under ambient condition and transferred into a 150 mL Teflon-lined stainless steel autoclave which was maintained at 140 °C for 20 h. The resulting sample was collected by centrifugation, washed by ethanol and deionized water, dried in air at 60 °C for 12 h. The $BiVO_4$ powder was submitted to a further calcination treatment at 300 °C for 2 h.

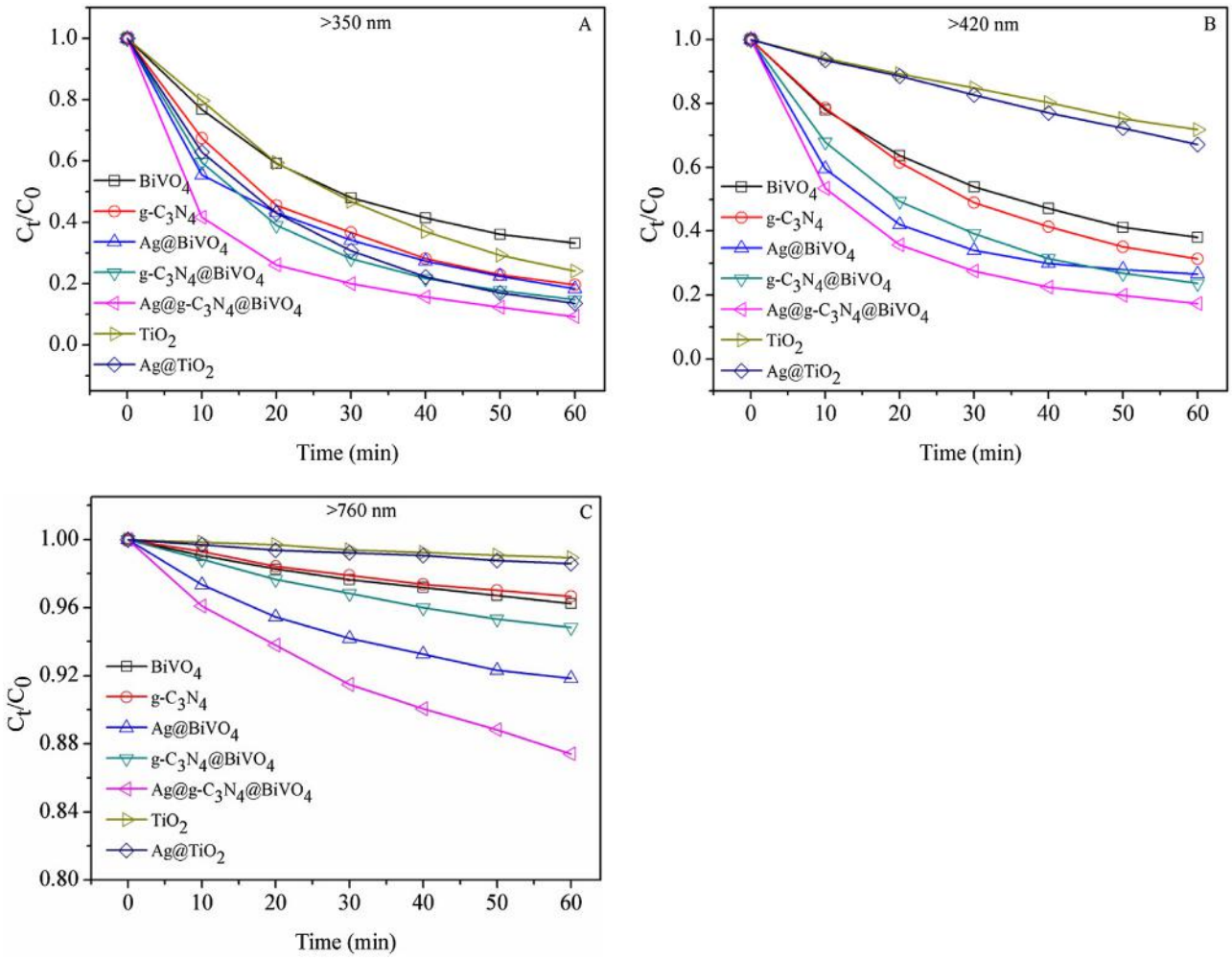

Fig. 1. Photocatalytic activities of the as-prepared photocatalysts under a 300W Xe lamp irradiation with different wavelength band-pass filters: (A) 350 nm, (B) 420 nm and (C) 760 nm.

2.4. Preparation of g-C_3N_4@$BiVO_4$ heterojunction

The g-C_3N_4@$BiVO_4$ heterojunction photocatalyst was fabricated by a wet-impregnation procedure as follows: At first, 0.5 g of as-prepared g-C_3N_4 was dispersed in a beaker containing 100 mL of methanol. The beaker was placed in an ultrasonic bath for 2 h to obtain homogeneous g-C_3N_4 dispersion. Afterwards, 0.5 g of $BiVO_4$ nanorods was added, continued sonicating for another 1 h and stirred in a fume hood for 24 h. After volatilization of the methanol, the resulting product was collected and dried at 60 °C for whole night. At last, g-C_3N_4(50 wt%)@$BiVO_4$ heterojunction was acquired after 2 h calcination at the temperature of 300 °C.

2.5. Preparation of Ag@$BiVO_4$ binary and Ag@g-C_3N_4@$BiVO_4$ ternary photocatalyst

The Ag(2 wt%)@$BiVO_4$ binary and Ag(2 wt%)@g-C_3N_4(50 wt%)@$BiVO_4$ ternary photocatalyst were prepared by a facile photodeposition process. In brief, 0.6 g of $BiVO_4$ or g-C_3N_4@$BiVO_4$ powder was dispersed into 80 mL de-ionized water with the aid of ultrasound. After 30 min, 1.14 mL of $AgNO_3$ solution (0.1 M) was added drop by drop to the resulted solution and maintained for another 0.5 h ultrasonic treatment. The solution was constantly stirred using a magnetic stirrer for 2 h at room temperature in dark. Then the above suspension was irradiated for 1 h with a 300 W Xe lamp under stirring while Ag^+ species were induced to form Ag nanoparticles on the surface of $BiVO_4$ or g-C_3N_4@$BiVO_4$. The precipitate was filtrated, washed with ethanol and de-ionized water for several times and dried at 60 °C for 24 h in a vacuum oven.

As a comparison, Ag(2 wt%)@TiO_2 photocatalyst was also prepared by the above method, where TiO_2 was used to replace the role of $BiVO_4$ or g-C_3N_4@$BiVO_4$ in Ag@$BiVO_4$ binary and Ag@g-C_3N_4@$BiVO_4$ ternary photocatalyst. For a more convenient narrative, g-C_3N_4(50 wt%)@ $BiVO_4$, Ag(2 wt%)@$BiVO_4$, Ag(2 wt%)@g-C_3N_4(50 wt%)@$BiVO_4$ and Ag(2 wt%)@TiO_2 were abbreviated as g-C_3N_4 @$BiVO_4$, Ag@$BiVO_4$, Ag@g-C_3N_4@$BiVO_4$ and Ag@TiO_2, respectively.

2.6. Characterization

The crystal structure and phase purity of the as-synthesized samples were analyzed by X-ray diffraction (XRD) using a Rigaku D/max 2500 v/pc X-ray diffractometer equipped with Cu-Kα radiation (λ = 0.15406 nm), employing a scanning rate of 0.1°s^{-1} in the 2θ range from 10 to 90°. Fourier transform infrared spectroscopy (FTIR) was collected on an IR Prestige-21 spectrometer using the standard KBr disk method. The morphologies were characterized by a field emission scanning electron microscope (FESEM, Hitachi S-4800) and a transmission electron microscopy (TEM, FEI Tecnai G20). The UV–vis absorption spectra were recorded on a UV–vis spectrometer (UV-4100, Shimadzu) with an integrating sphere

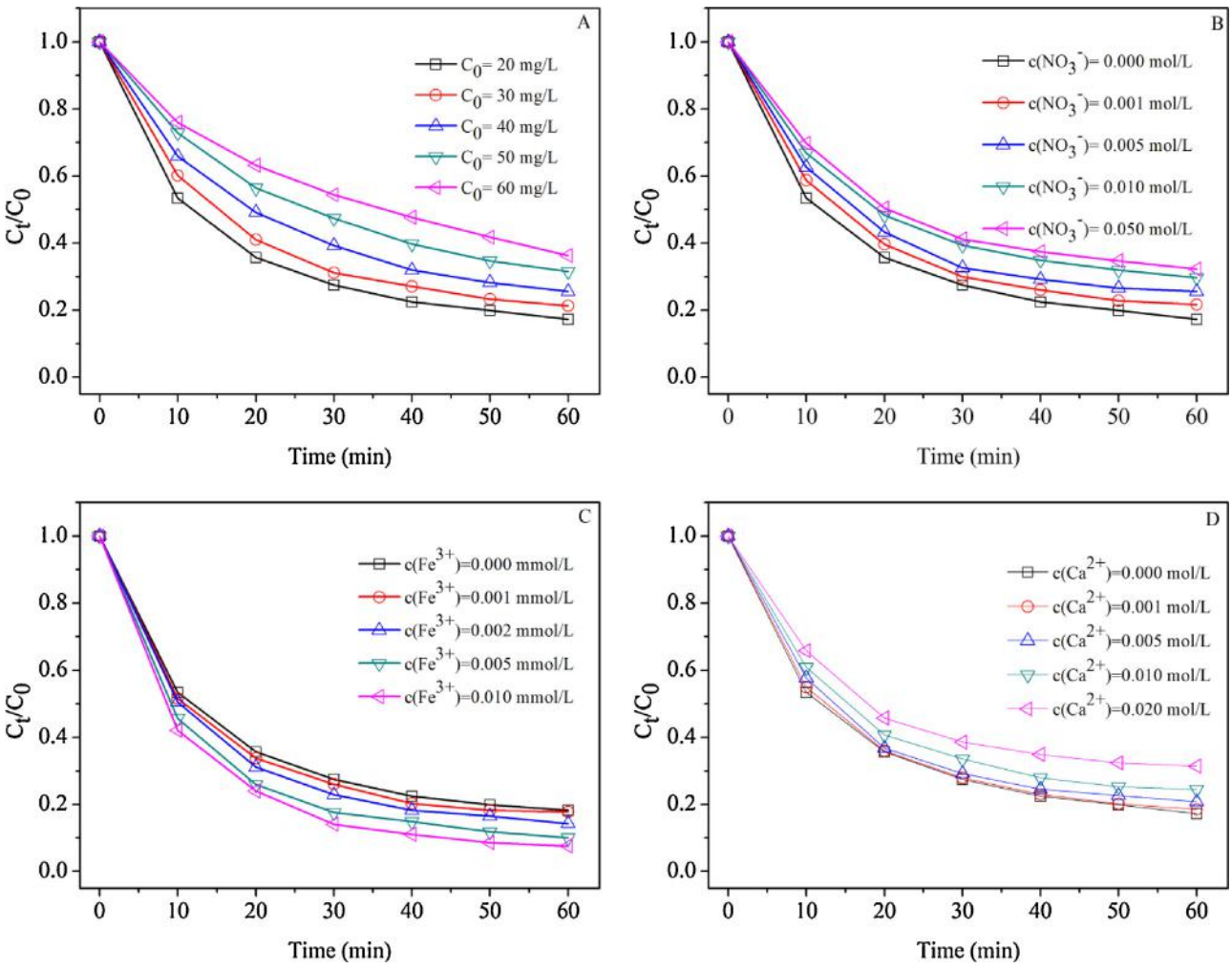

Fig. 2. Effect of the following factors on the degradation of TC over Ag@g-C_3N_4@$BiVO_4$ nanocomposite under visible light irradiation (λ > 420 nm): (A) initial TC concentration; (B) coexisting cation ion, NO_3^-; (C) coexisting anion ion, Fe^{3+} and (D) coexisting anion ion, Ca^{2+}.

attachment within the range of 200–1200 nm. The X-ray photoelectron spectroscopy (XPS) was employed to determine the chemical states of elements using a Thermo ESCALAB 250XI spectrometer with Al Kα source. The photoluminescence (PL) spectroscopy was obtained by a Hitachi-4600 fluorescence spectrometer. The N_2 physical absorption measurements were carried out at 77 K on a TRISTAR-3000 analytical system. The specific surface area was calculated by Brunauer-Emmett-Teller (BET) method. The electron spin resonce (ESR) measurements of the free radicals was examined by using 5,5-dimethyl-l-pyrroline *N*-oxide (DMPO) as a probe on a Bruker ER200-SRC spectrometer under visible light irradiation (λ > 420 nm).

2.7. Assessment of photocatalytic activities and photostability

The photocatalytc activities of the obtained samples were investigated via the degradation of TC in aqueous solution under a 300W Xe lamp irradiation with different wavelength band-pass filters. At first, a 100 mL of TC solution with an initial concentration of 20 mg/L was mixed with 0.03 g of solid catalyst. Then the mixed solution was stirred in dark for 30 min to reach the adsorption–desorption equilibrium. After that, the suspension was exposed to the 300W Xe lamp. At given time interval after initiation of the light irradiation, 4 mL of the samples were collected into centrifuge tubes, centrifuged at 10,000 rpm for 10 min. The residual concentration was measured by a Shimadzu UV–vis spectrophotometer with the maximal absorption wavelength of TC, whose characteristic absorption peak as 357 nm. To evaluate the photostability of the catalysts, four successive cycle tests were implemented over pure $BiVO_4$ and Ag@g-C_3N_4@$BiVO_4$ under simulated light or visible light (λ > 420 nm). After a photocatalytic experiment, the solid photocatalyst was recovered by washing thoroughly with distilled water, dried at 60 °C for 12 h and subjected to the next cycle.

3. Results and discussion

3.1. Photocatalytic performance

3.1.1. Photocatalytic behaviors under different light wavelength irradiation

Tetracycline (TC), a typical antibiotic, was chosen as a representative refractory pollutant to evaluate the corresponding photocatalytic activities. Before light irradiation, a dark adsorption experiment was carried out to investigate the adsorption-desorption equilibrium. As revealed in Table 1, there was no significant increase of adsorption for all the samples after 30 min dark reaction, suggesting that the adsorption-desorption equilibrium between the catalyst and TC molecules had been established. As a result, before light irradiation, 30 min of dark adsorption was applied to all the photodecomposition process.

Full-spectrum photocatalysis can make the best use of natural sunlight in environmental remediation process. In this study, the

Table 1
Adsorption and photocatalytic activities of the as-prepared photocatalysts under different irradiation conditions (A_t, represents for adsorption ability and η, represents for degradation efficiency).

Sample	Adsorption			>350 nm	>420 nm	>760 nm
	A_{10} (%)	A_{30} (%)	A_{60} (%)	η (%)	η (%)	η (%)
TiO_2	0.14	0.22	0.23	75.89	28.22	1.06
Ag@TiO_2	0.25	0.28	0.28	86.51	32.91	1.41
$BiVO_4$	8.46	12.42	12.40	66.73	61.91	3.76
g-C_3N_4	0.29	0.30	0.31	80.41	68.66	3.33
Ag@$BiVO_4$	7.59	10.75	10.78	81.74	73.42	8.15
g-C_3N_4@$BiVO_4$	4.56	6.34	6.36	85.27	76.32	5.17
Ag@g-C_3N_4@$BiVO_4$	3.85	7.73	7.75	90.76	82.75	12.59

degradation experiment of TC was performed under a 300W Xe lamp with no (> 350 nm, as simulated solar light) or different wavelength band-pass filters (>420 nm, as visible light and >760 nm, as near infrared light). Fig. 1 illustrates the photodecomposition efficiency changes in terms of TC relative concentration (C_t/C_0) as a function of irradiation time over pure $BiVO_4$, pure g-C_3N_4 and Ag and g-C_3N_4 single or co-modified $BiVO_4$ nanocomposites. For comparison, commercial TiO_2 and Ag@TiO_2 were also taken into consideration. As shown in Fig. 1A and Table 1, only 66.73% of TC was degraded in 60 min over pure $BiVO_4$ with no light cut-off filter (λ > 350 nm). The removal rate could reach to 81.74% when Ag nanoparticles were introduced. The presence of g-C_3N_4 also significantly enhanced the photoactivity of single $BiVO_4$, approximately 19% degradation efficiency enhancement, which might be ascribed to the forming heterojunction between g-C_3N_4 and $BiVO_4$. Compared with single-component and two-component samples, the ternary Ag@g-C_3N_4@$BiVO_4$ nanocomposite exhibited the highest photocatalytic activity and TC concentration was reduced by 90.76%. Moreover, Ag@g-C_3N_4@$BiVO_4$ sample also showed a higher removal efficiency than TiO_2 (75.89%) and Ag@TiO_2 (86.51%). When all the prepared photocatalysts were exposed to visible light with a 420 nm cutoff filter (Fig. 1B), a certain degree decrease of degradation efficiency could be observed due to the declining light intensity. Although, the degradation efficiency of TC reduced 8.01% for Ag@g-C_3N_4@$BiVO_4$ ternary photocatalyst, it still presented as the optimum photoactivity. The corresponding degradation rates of all the samples could be listed as following order: Ag@g-C_3N_4@$BiVO_4$ > g-C_3N_4@$BiVO_4$ > Ag@ $BiVO_4$ > g-C_3N_4 > $BiVO_4$ > Ag@TiO_2 > TiO_2. It was worthy to notice that the photocatalytic activity of Ag@TiO_2 and TiO_2 drastically decreased under visible light irradiation, indicating the lower visible-light response. The above information demonstrated the visible-light photoactivity of $BiVO_4$ and modified $BiVO_4$ photocatalysts was higher, which exhibited more potential in practical applications. With the light wavelength increasing over 760 nm (Fig. 1C, near infrared light), the photocatalytic performance of all the catalysts remarkably declined, because long wavelength didn't excite their photogenerated charges. Even so, Ag nanoparticles and g-C_3N_4 co-modified $BiVO_4$ always possessed much higher photocatalytic activity than single or binary $BiVO_4$ catalysts. It demonstrated that Ag@g-C_3N_4@$BiVO_4$ nanocomposite showed superior photocatalytic performance under full wavelength range irradiation due to the synergistic effect among three semiconductors and stronger absorption in the light region, leading to the efficient photo-induced electron-hole pairs separation.

3.1.2. *Effects of initial TC concentrations and coexisting ions*

For the viewpoint of practical wastewater treatment, initial pollutant concentration is a vital point to acquire the satisfying removal efficiency. Furthermore, it is well-known that inorganic salts were common in waters, thus it is necessary to explore their effects on TC removal process. Herein, we chose three general inorganic ions: NO_3^-, Fe^{3+} and Ca^{2+}. It should be noted that all

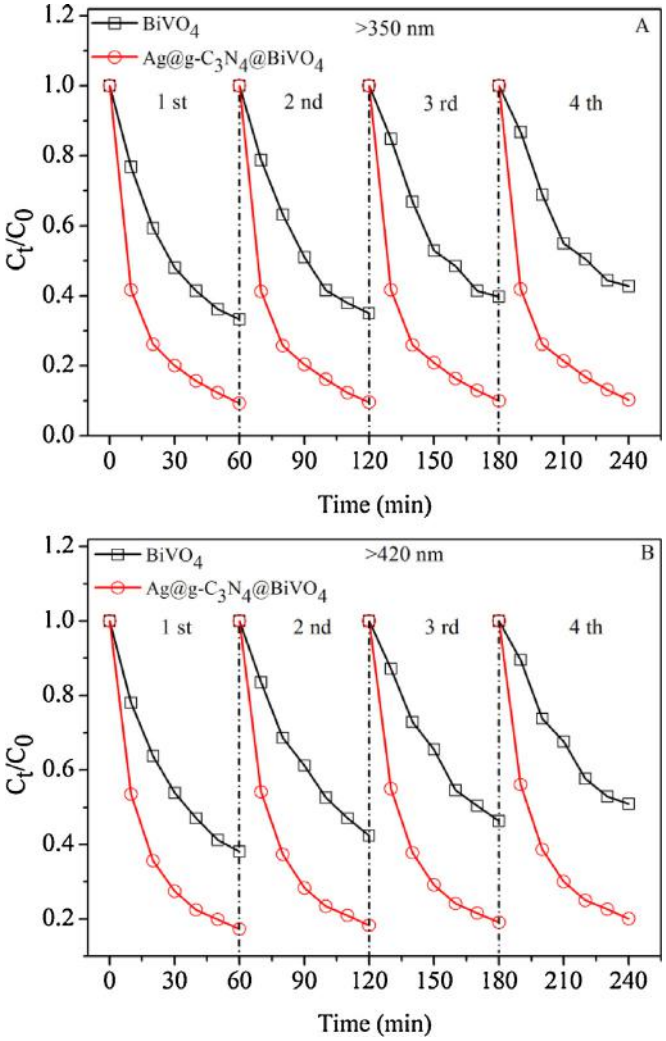

Fig. 3. Cycling runs for the photocatalytic degradation of TC in the presence of $BiVO_4$ or Ag@g-C_3N_4@$BiVO_4$ under a 300W Xe lamp irradiation with no or a 420 nm wavelength band-pass filter.

the parameters investigation experiments were performed over Ag@g-C_3N_4@$BiVO_4$ nanocomposite under visible light irradiation (λ > 420 nm).

The effect of initial TC concentrations was investigated with different initial concentrations: 20, 30, 40, 50 and 60 mg/L, and the results were illustrated in Fig. 2A. Negative effect could be detected along with the increasing TC concentrations, and the removal efficiency decreased from initial 82.74% (20 mg/L) to later 63.69% (60 mg/L). The reasons could be explained from two aspects: for one, higher TC concentration would result in the decease of the path length of photon entering the TC solution [35]. For the

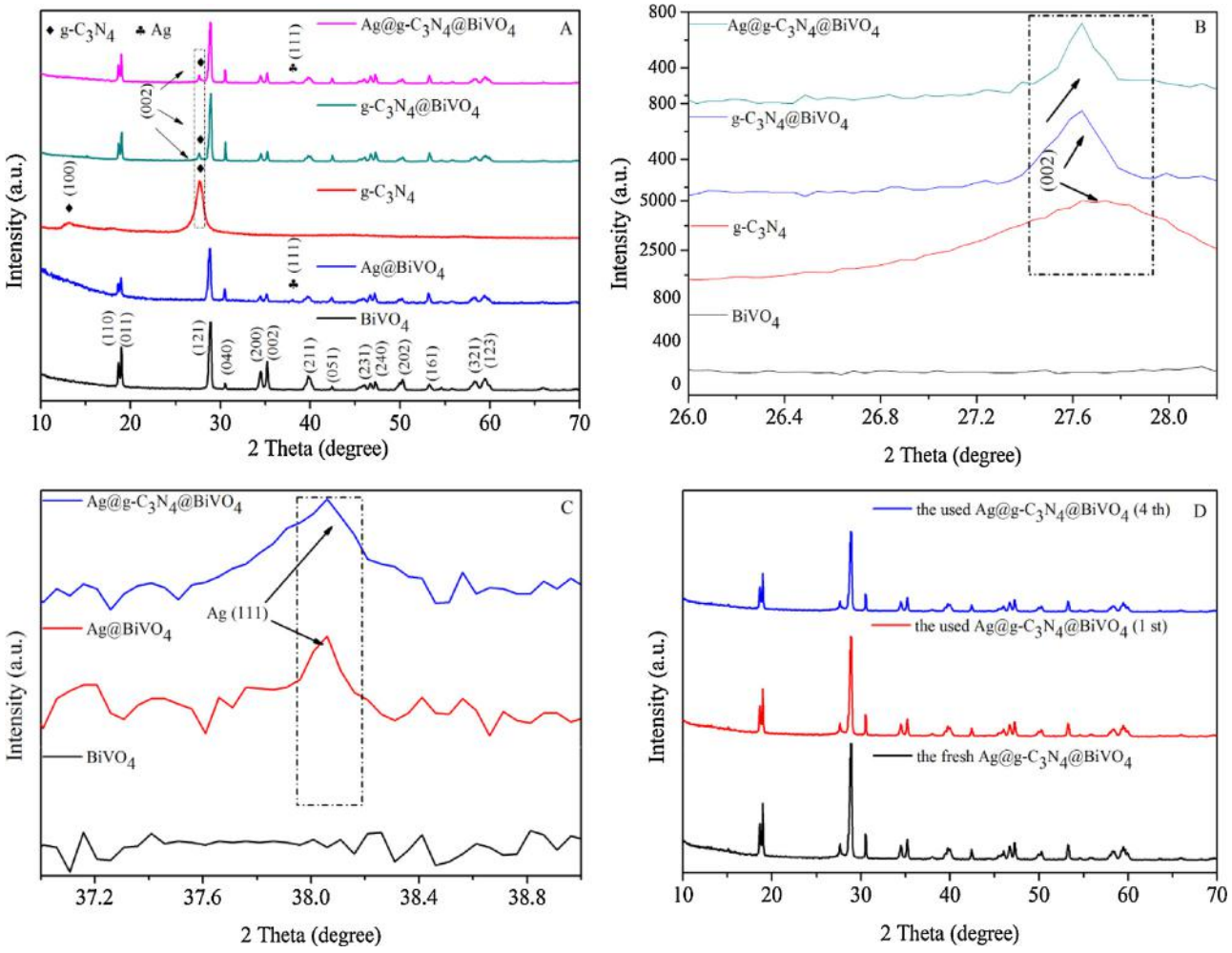

Fig. 4. XRD patterns of the as-prepared samples (A), the corresponding diffraction peaks of g-C_3N_4 (B), metallic Ag (C) and the fresh and Ag@g-C_3N_4@$BiVO_4$ nanocomposite (D).

other, TC molecules could be degraded into other intermediates or directly into CO_2 and H_2O. Nevertheless, the generated intermediates might compete the limited reaction interspace with TC molecules, and this competitiveness force would gradually strengthen with the increasing TC concentrations [37,38]. It is notable that Ag@g-C_3N_4@$BiVO_4$ nanocomposite also displayed relatively high photocatalytic activity towards TC degradation, only about 19.05% loss from 20 mg/L to 60 mg/L unlike the significant reduction reported in previous literatures [39], indicating that Ag@g-C_3N_4@$BiVO_4$ possessed great potential for TC or other refractory pollutants removal at relatively higher concentration.

From Fig. 2B, the coexisting cation ion, NO_3^-, exhibited the inhibitory effect in the TC degradation process. Along with the increasing NO_3^- ion strength ($NaNO_3$ was chosen as the provider), the TC removal rate synchronously decreased, where there were about 14.97% loss in the presence of 0.05 mol/L NO_3^-. This phenomenon might be attributed to the increased charge of NO_3^- ions, which augmented the electrostatic repulsion between ions, rendered the surface adsorption site of the catalyst and reduced the adsorption rate [40]. The effect of $Fe^{3+}$was revealed in Fig. 2C. The Fe^{3+} contents in the TC solution were setup as 0, 0.001, 0.002, 0.005 and 0.010 mmol/L by adding the corresponding $Fe(NO_3)_3{\cdot}9H_2O$, respectively. In contrast to the negative effect of NO_3^- on TC degradation, the emergence of Fe^{3+} simultaneously enhanced the whole photocatalytic performance. And the increasing range was much higher than that the suppression of NO_3^-. TC removal efficiency was 82.75% without the addition of $Fe(NO_3)_3{\cdot}9H_2O$. With the increasing $Fe(NO_3)_3{\cdot}9H_2O$ dosage, it raised and reached to be 92.94% in the presence of 0.010 mmol/L of Fe^{3+}. According to previous studies, Fe^{3+} was an important inorganic photosensitive substance and it could adsorb the light to produce active species, $^{\bullet}OH$, under weakly acidic solution. The generated $^{\bullet}OH$ could accelerate the photo-oxidation process, herein, it could speed up the removal rate of TC degradation [41]. In addition, the photogenerated electrons and holes can be trapped by Fe^{3+}, which can be turned into Fe^{2+} and Fe^{4+} ions by trapping photogenerated electrons and holes, hence, holding up the recombination process [42]. Therefore, the introduction of Fe^{3+} significantly promoted the degradation process. Different from the promotion role of Fe^{3+}, the addition of Ca^{2+} suppressed the photocatalytic process to a certain extent (Fig. 2D). The increasing dosage of $CaCl_2$ will result in the higher photoactivity inhabitation. The same phenomenon was also verified by previous study [40,43]. The intrinsic reason could be assigned to the fact that Ca^{2+} binds to tetracycline to form the metal complexes. Meanwhile, the formation of metal intermediates might affect the photocatalytic degradation process of TC.

3.1.3. Evaluation of photostability

The stability and recyclability of the photocatalysts are significant factors in their practical applications. In this work, the photostability of pure $BiVO_4$ and Ag@g-C_3N_4@$BiVO_4$ was investigated under simulated light (no cutoff filter) or visible light

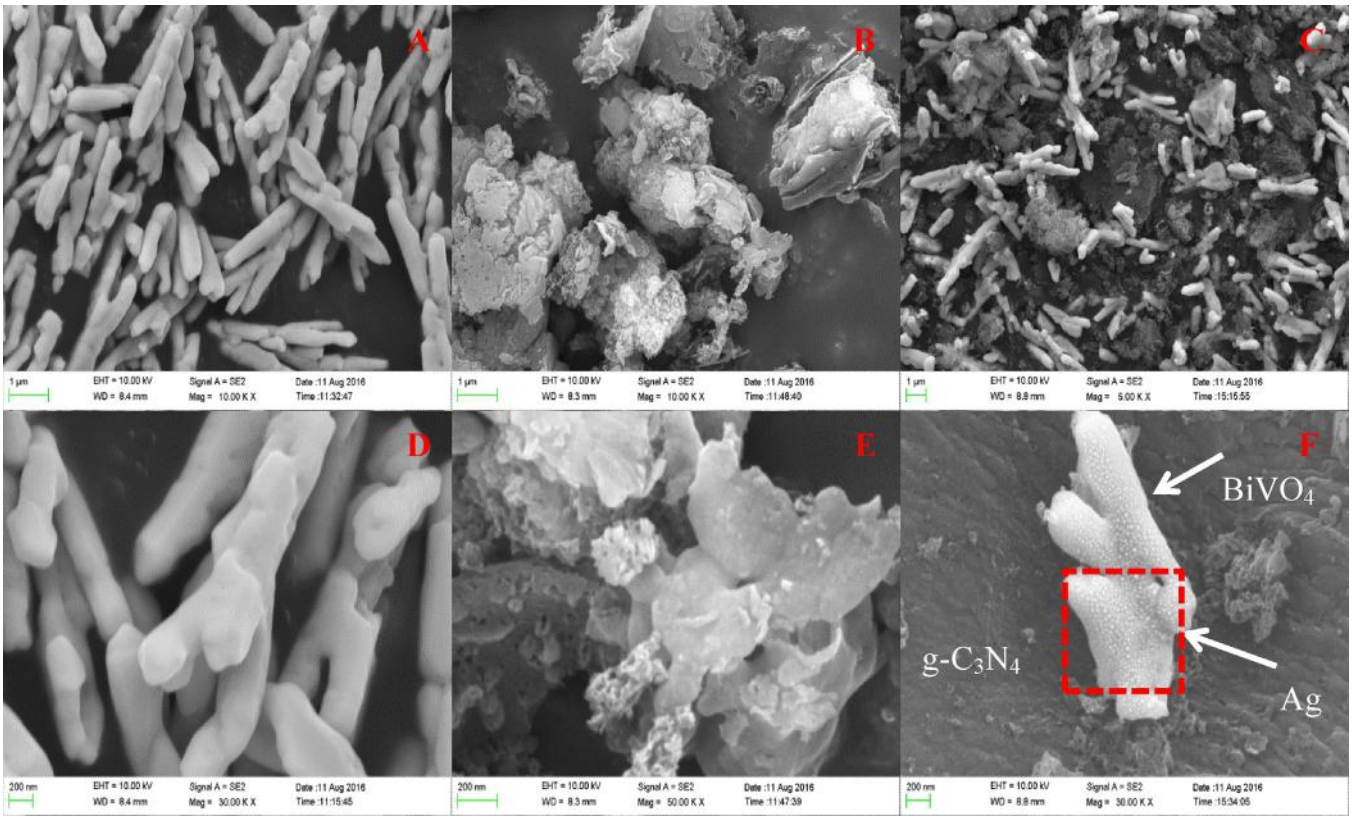

Fig. 5. SEM images of (A, D) $BiVO_4$, (B, E) g-C_3N_4 and (C, F) Ag@g-C_3N_4@$BiVO_4$.

irradiation (λ > 420 nm). As presented in Fig. 3A and B, it could be observed that the photocatalytic activity of Ag@g-C_3N_4@$BiVO_4$ catalyst was little change, while the degradation efficiency for pure $BiVO_4$ existed a significant loss. There were about 9.43% (>350 nm) and 12.78% (>420 nm) reduction in the corresponding efficiency towards TC decomposition over $BiVO_4$. The above results confirmed that Ag@g-C_3N_4@$BiVO_4$ was effective and stability during the photocatalysis, and obviously, the co-modified method enhanced the single-component $BiVO_4$ for both photocatalytic performance and photostabilty. Furthermore, XRD patterns of the fresh and used Ag@g-C_3N_4@$BiVO_4$ sample in Fig. 4D displayed that no discernable changes were perceived about the phase structure of Ag@g-C_3N_4@$BiVO_4$ after repeated photocatalytic reactions, indicating that the sample could work as a stable and efficient photocatalyst for practical application in wastewater treatment.

3.2. Characterization of the photocatalyst

Powder XRD patterns of pure $BiVO_4$, pure g-C_3N_4, binary and ternary nanocomposites are shown in Fig. 4A. The structure of $BiVO_4$ nanorods was detected to be in monoclinic phase of $BiVO_4$ (JCPDS Card No. 14-0688 [34]). For pure g-C_3N_4, two distinct diffraction peaks at 2θ values of 12.77° and 27.63° were indexed as the (100) and (002) planes of the graphite-like structure of g-C_3N_4 [20,26], which were corresponding to the in-planar structural packing motif and the interlayer stacking of the aromatic system. For two binary samples: Ag@$BiVO_4$ and g-C_3N_4@$BiVO_4$ as well as one ternary Ag@g-C_3N_4@$BiVO_4$ sample, the similar XRD patterns as $BiVO_4$ were also found. That is to say, the introduction of Ag nanoparticles and g-C_3N_4 in the nanocomposite photocatalysts had no obvious influence on their crystalline structures. Notably, the typical diffraction peak (27.63°) of g-C_3N_4 was also perceived in the XRD patterns of g-C_3N_4@$BiVO_4$ and Ag@g-C_3N_4@$BiVO_4$. For better visibility, the peak corresponded to g-C_3N_4 was picked out in smaller areas (Fig. 4B). The peaks belonged to metallic Ag could not been observed due to the small particles sizes and low doping concentration of Ag. Under the state of amplification (Fig. 4C), a weak characteristic peak at 2θ value of 38.12° could be attributed to the (111) crystal plane of metallic Ag, which was in good accordance with previous verification method [44]. No other new diffraction peaks were observed in all samples, implying that the whole catalysts maintained the pure phase and no impurities formation in the preparation.

The morphology and microstructure of $BiVO_4$, g-C_3N_4 and Ag@g-C_3N_4@$BiVO_4$ were investigated by SEM technology. As seen from Fig. 5A and D, $BiVO_4$ presented as nanorods structure with smooth surface. Fig. 5B and E the synthesized g-C_3N_4 was layered consist of stacked nanosheets. Examination of Ag@g-C_3N_4@$BiVO_4$ ternary composite (Fig. 5C and F), both layered g-C_3N_4 and $BiVO_4$ nanorods were found, indicating good affinity between these materials. While in a magnified version, the surface of $BiVO_4$ was also comprised of many tiny nanoparticles, which should be assigned to the formation of metallic Ag on the surface. The layered g-C_3N_4 presented as the substrate of Ag and $BiVO_4$. Additional cross-section elemental mappings combined with EDS analysis for pure $BiVO_4$ and Ag@g-C_3N_4@$BiVO_4$ were also performed (Fig. 6). For pure $BiVO_4$ (Fig. 6A–F), Bi, V, O elements were all existed, and the molar ratio of Bi/V was estimated to 1.05:1, which was close to the stoichiometric ratio of Bi/V in the preparation. As obtained from Fig. 6G–N, C, N, Bi, O, V and Ag were all presented. The weight ratio of Ag in the nanocomposite was calculated to 1.96%, which was in good agreement with the amount of the synthesis. Specially, the Ag distributed throughout the film, suggesting that metallic Ag had been evenly dispersed on the surface of $BiVO_4$ and g-C_3N_4. In comparison with pure $BiVO_4$, the EDS spectrum of Ag@g-C_3N_4@$BiVO_4$ had weaker peaks of Bi and V than those of $BiVO_4$, while the amount

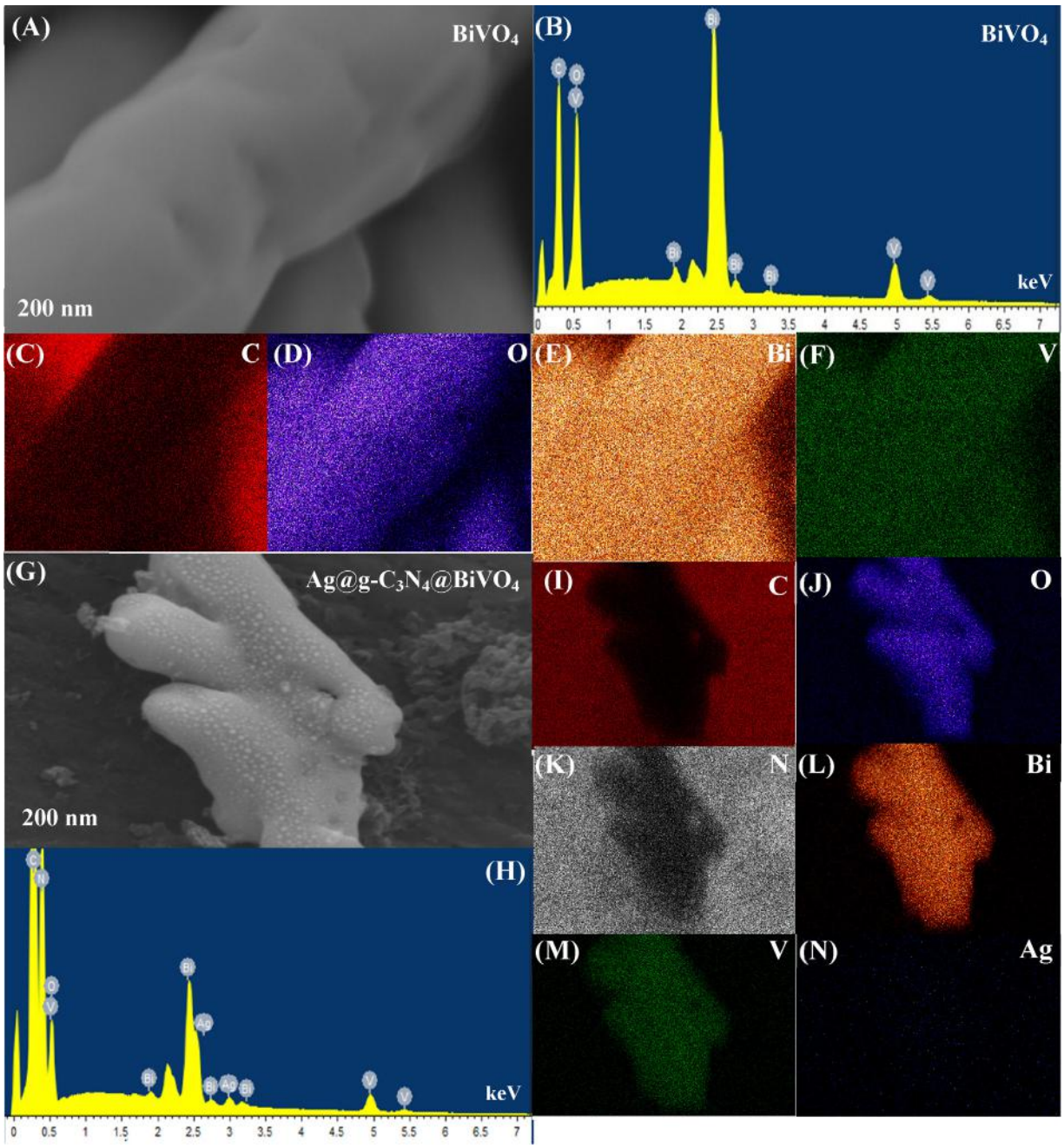

Fig. 6. SEM-EDS elemental mapping images of (A–F) $BiVO_4$ and (G–N) Ag@g-C_3N_4@$BiVO_4$ nanocomposite.

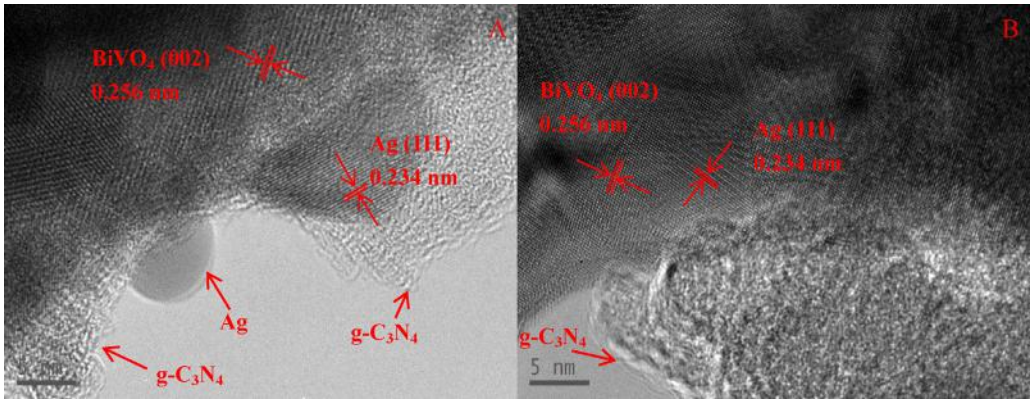

Fig. 7. HRTEM images analysis of Ag@g-C_3N_4@$BiVO_4$ nanocomposite.

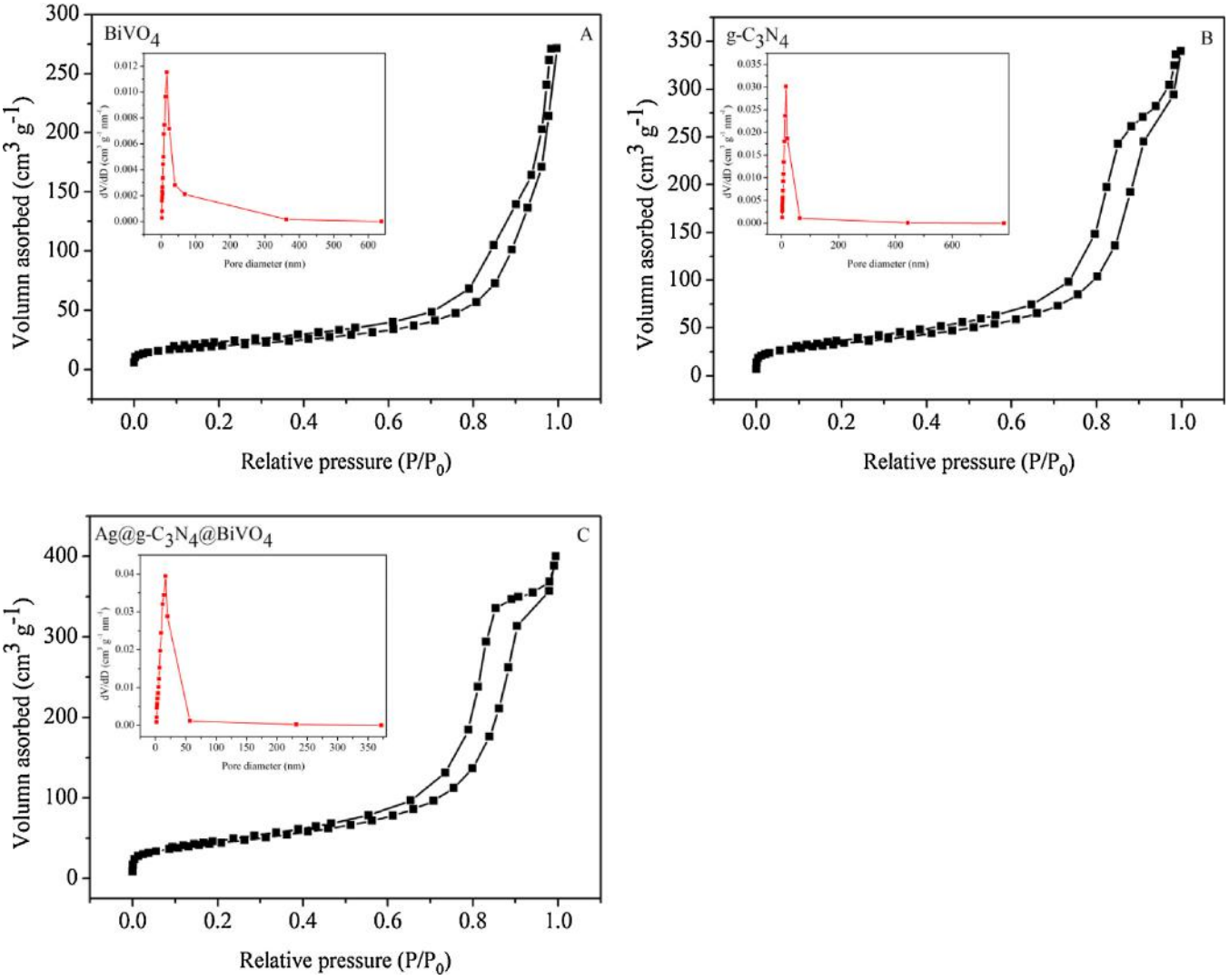

Fig. 8. Nitrogen sorption isotherm and Barrett-Joyner-Halenda (BJH) pore size distribution plot (inset) of pure $BiVO_4$ (A), pure g-C_3N_4 (B) and Ag@g-C_3N_4@$BiVO_4$ (C).

of C and N increased to a great extent. In order to further determine the successful introduction of Ag and g-C_3N_4 in the ternary system, Ag@g-C_3N_4@$BiVO_4$ was further observed by HRETM, and the relative results are showed in Fig. 7. The interplanner spacings of 0.256 nm were clearly observed, which corresponded to (002) crystallographic planes of $BiVO_4$ (JCPDS Card No. 14-0688). The lattice fringe of 0.234 nm belonged to the (111) plane of metallic Ag. The g-C_3N_4 nanosheets were served as the substrate for metallic Ag and $BiVO_4$, and were marked out in Fig. 7A–B. Based on the above analyses, it could be concluded that metallic Ag and g-C_3N_4 were successfully introduced into Ag@g-C_3N_4@$BiVO_4$ and the well connection among Ag, g-C_3N_4 and $BiVO_4$ was built, which promoted the effective electrons and holes separation in the ternary system.

The specific surface area and pore characteristic of Ag@g-C_3N_4@$BiVO_4$ ternary nanocomposite as well as pure $BiVO_4$ and g-C_3N_4 were measured through the N_2 sorption analysis. As depicted in Table 2, the BET surface areas of $BiVO_4$, g-C_3N_4 and Ag@g-C_3N_4@$BiVO_4$ were calculated to be ca. 70.234, 120.255 and 157.620 $m^2\,g^{-1}$, respectively. Compared with pure g-C_3N_4, Ag@g-C_3N_4@$BiVO_4$ even showed a larger specific surface area, which could be ascribed to the fact that g-C_3N_4 layered structure was exploited into nanosheets in the Ag@g-C_3N_4@$BiVO_4$ preparation procedure. The pore-size distribution of the samples were also estimated using the Barrett-Joyner-Halenda (BJH) method from desorption branch of the isotherm and displayed in the inset of Fig. 8. Combined with the dark reaction, bigger specific area and pore volume played an important role in the enhancement of photoactivity instead of the improvement of adsorption ability.

Table 2
Surface area, pore size and pore volume parameters for pure $BiVO_4$, pure g-C_3N_4 and Ag@g-C_3N_4@$BiVO_4$ nanocomposite.

Samples	Surface area[a] (m^2/g)	Pore size[b] (nm)	V_t[c] (cm^3/g)
$BiVO_4$	70.234	16.597	0.432
g-C_3N_4	120.255	15.548	0.545
Ag@g-C_3N_4@$BiVO_4$	157.620	16.551	0.639

[a] Measured using N_2 adsorption with the Brunauer-Emmett-Teller (BET) method.
[b] Pore size in diameter calculated by the desorption data using Barrett-Joyner-Halenda (BJH) method.
[c] Total pore volume determined at $P/P_0 = 0.99$.

The composition and structure of the catalysts could be also confirmed by FT-IR spectra. As displayed in Fig. 9, the peaks located at 1641, 1243, 1320, 1409, and 1570 cm^{-1} belonged to the typical stretching vibration modes of the g-C_3N_4 heterocycles. A sharp absorption peak at 807 cm^{-1} is assignable to the characteristic breathing mode of triazine units [11]. The absorption band at 651 cm^{-1} was attributable to the bending vibration band of Bi-O group [45]. The characteristic peaks of $BiVO_4$ and g-C_3N_4 could

also be perceived were commonly presented for the corresponding $BiVO_4$ or g-C_3N_4-containing samples. All the main characteristic peaks in the complex samples moved to a lower wavenumber, suggesting that the successful synthesis had been realized. For Ag@$BiVO_4$, no discernable discrepancy could be observed, due to the small amount of metallic Ag in the nanocomposites, and it also inferred that the introduction of Ag didn't change the initial chemical structure of $BiVO_4$.

The surface chemical composition and electronic state of Ag@g-C_3N_4@$BiVO_4$ nanocomoposite was determined by the X-ray photoelectron spectroscopy (XPS) (Fig. 10). As revealed in Fig. 10A, six elements: C, N, Bi, V, O and Ag were detected in the XPS survey spectrum of Ag@g-C_3N_4@$BiVO_4$. High resolution spectra of C 1s (Fig. 10B) at 284.84 eV and 287.72 eV could be attributed to the C-C bonds and the tertiary carbon C-$(N)_3$ [36]. Two characteristic peaks located at 398.82 eV and 400.01 eV (Fig. 10C) might due to N atoms sp^2-bonded to two carbon atoms (C=N–C) and bridging nitrogen atoms N-$(C)_3$, respectively [46]. The Bi 4f XPS spectrum is shown in Fig. 10D, two individual peaks with the binding energy of 158.79 eV and 164.81 eV could be corresponded to Bi $4f_{7/2}$ and Bi $4f_{5/2}$, respectively [17]. Two main peaks (Fig. 10E) appearing at the binding energies of 516.82 eV and 524.17 eV belonged to V $2p_{3/2}$ and V $2p_{1/2}$, respectively [24]. As displayed in Fig. 10F, typical O 1s spectrum exhibits the predominant characteristic peak at 529.92 eV. Fig. 10G shows the Ag 3d spectrum with two individual peaks, on peak located at 368.03 eV for Ag $3d_{5/2}$ and the other one with the binding energy of 374.01 eV is assigned to Ag $3d_{3/2}$ [32]. The FTIR and XPS results coincided well with the XRD, SEM and HRTEM analysis.

UV/vis diffuse reflectance spectrum (DRS) was measured to evaluate the optical bandgap and absorption properties of the as-prepared photocatalysts. As illustrated in Fig. 11A, the optical absorption edge was estimated to be about 517 nm for $BiVO_4$ and 453 nm for g-C_3N_4. After coupling $BiVO_4$ and g-C_3N_4, the absorption edge gradually moved to longer edge, due to the forming heterojunction between two semiconductors. Meanwhile, the obtained Ag@$BiVO_4$ sample exhibited a broad absorption in visible light region, which could be assigned to the surface plasmon resonance (SPR) effect of spatially confined electrons in Ag nanoparticles. The Ag nanoparticles and g-C_3N_4 co-modified $BiVO_4$ showed distinctly enhanced visible light absorption extending to 1100 nm (NIR region) as compared with all other samples, coinciding with the results of photoactivity test, thus synergetic effect in the ternary system worked. The band gap energies of semiconductors can be Kubelka-Munk equation [28]:

$$\alpha h\upsilon = A(h\upsilon - Eg)^{n/2} \quad (1)$$

where α represents the absorption coefficient, υ is the light frequency, Eg is the band gap energy, A is a constant and n depends on the characteristics of the transition in a semiconductor. The value of n for $BiVO_4$ and g-C_3N_4 was both determined to be 4 because of an indirect optical transition type. Thus, as shown in Fig. 11B, the optical bandgap of $BiVO_4$ and g-C_3N_4 was calculated to be 2.40 eV and 2.74 eV, respectively, which are close to the corresponding values in previous reports [21,31]. Furthermore, the conduction band (CB) and valence band (VB) edge position of a semiconductor material could be calculated by the equations as follows [47]:

$$E_{CB} = X\text{-}E^c\text{-}0.5E_g \quad (2)$$

$$E_{VB} = E_{CB} + E_g \quad (3)$$

where X is the electronegativity of the semiconductor, E^e is the energy of free electrons on the hydrogen scale (~4.5 eV vs NHE), and the CB and VB potentials of g-C_3N_4 are calculated to be −1.23 eV and +1.51 eV, respectively [11,36]. The CB and VB potentials of $BiVO_4$ are estimated to be +0.46 eV and +2.86 eV [34], respectively.

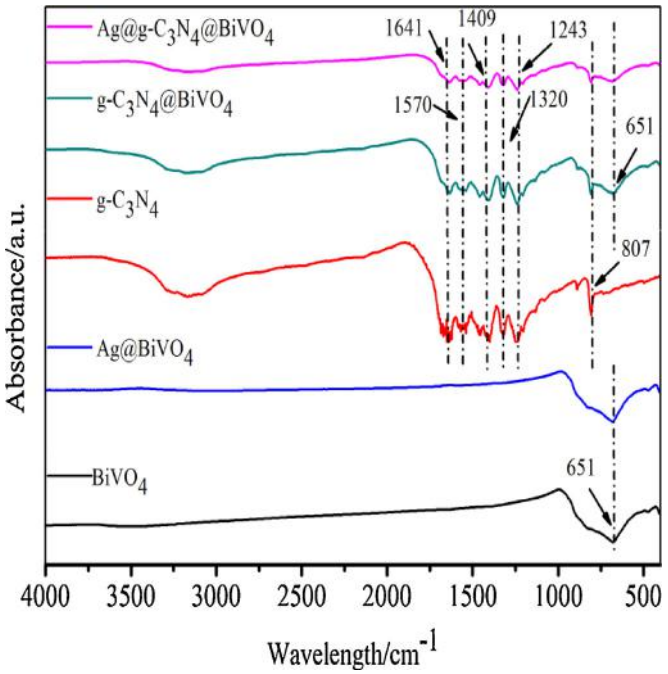

Fig. 9. FTIR spectra of the as-prepared Ag nanoparticles and g-C_3N_4 co-modified $BiVO_4$ samples.

3.3. Proposed enhancement mechanism of Ag@g-C_3N_4@$BiVO_4$ photocatalytic activity

In order to elucidate the reaction mechanism in depth, the main active species formed during the reaction process were identified by a hole and free radical trapping experiments over $BiVO_4$ and Ag@g-C_3N_4@$BiVO_4$ under identical conditions (herein, visible light, λ > 420 nm). In this study, 1.4-benzoquinone (BQ) was utilized for superoxide radical ($^{\bullet}O_2^-$) scavenger, ethylenediaminetraacetic acid disodium (EDTA-2Na) for hole (h^+) scavenger and Isopropanol (IPA) for hydroxyl radical ($^{\bullet}OH$) scavenger [35,38]. In addition, N_2 purging experiments were also carried out to confirm the role of $^{\bullet}O_2^-$ in the photocatalytic system. The experimental results (Fig. 12A–B) showed that the addition of BQ or EDTA-2Na caused obviously deactivation of the $BiVO_4$ photocatalyst. The removal efficiency of TC declined from 61.91% (air-equilibrated condition) to 23.70% with N_2 purging, which demonstrated the significant role of $^{\bullet}O_2^-$ in the photocatalytic process. Especially, the photocatalytic activity was almost inhibited by 1 mmol of EDTA-2Na and the degradation rate of TC reduced from 61.91% to 4.65%. Simultaneously, the addition of 1 mmol of IPA had little effect on the decomposition of TC, indicating that fewer $^{\bullet}OH$ was involved in the reaction procedure. Therefore, the major active species for pure $BiVO_4$ should be $^{\bullet}O_2^-$ and h^+. The metallic Ag and g-C_3N_4 co-modified $BiVO_4$ nanocomposite exhibited a significant discrepancy in active species production. As displayed in Fig. 12C–D, the photocatalytic activity of Ag@g-C_3N_4@$BiVO_4$ after 60 min irradiation decreased 57.19% with the addition of BQ. Furthermore, a large-scale reduction for TC degradation was observed in the presence of EDTA-2Na (44.18% loss after 60 min) and IPA (26.90% reduction after 60 min). Thus, it could infer that, $^{\bullet}O_2^-$, h^+ and $^{\bullet}OH$ all played an important role in the photodegradation process over Ag@g-C_3N_4@$BiVO_4$. Based on above investigations, it could be preliminarily concluded that the enhancement of photocatalytic performance by Ag@g-C_3N_4@$BiVO_4$ should be the coexist effect of $^{\bullet}O_2^-$, h^+ and $^{\bullet}OH$, while only $^{\bullet}O_2^-$ and h^+ were pivotal for the TC degradation for single $BiVO_4$. To further identify the radical generation in the photocatalytic system under visible light irra-

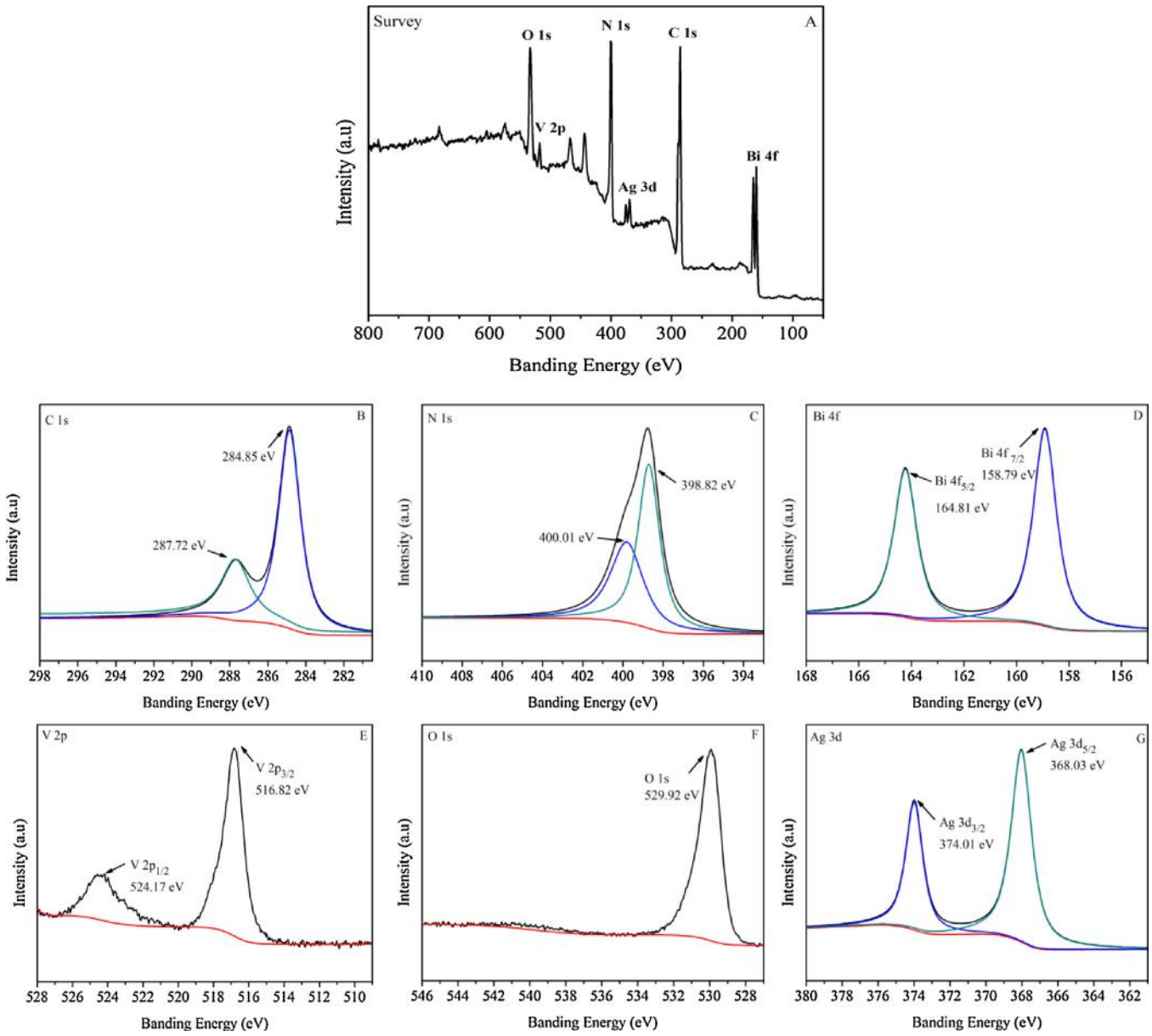

Fig. 10. XPS spectra of Ag@g-C_3N_4@$BiVO_4$ nanocomposite: (A) survey, (B) C 1s, (C) N 1s, (D) Bi 4f, (E) V 2p, (F) O 1s and (G) Ag 3d.

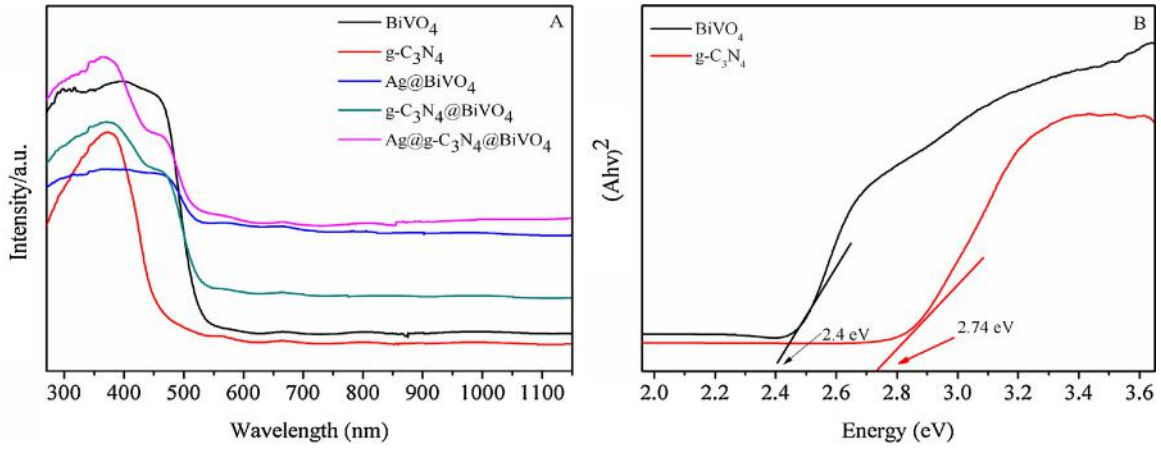

Fig. 11. UV–vis diffuse reflectance spectra of the as-prepared photocatalysts (A) and the optical bandgap of pure $BiVO_4$ and g-C_3N_4 (B).

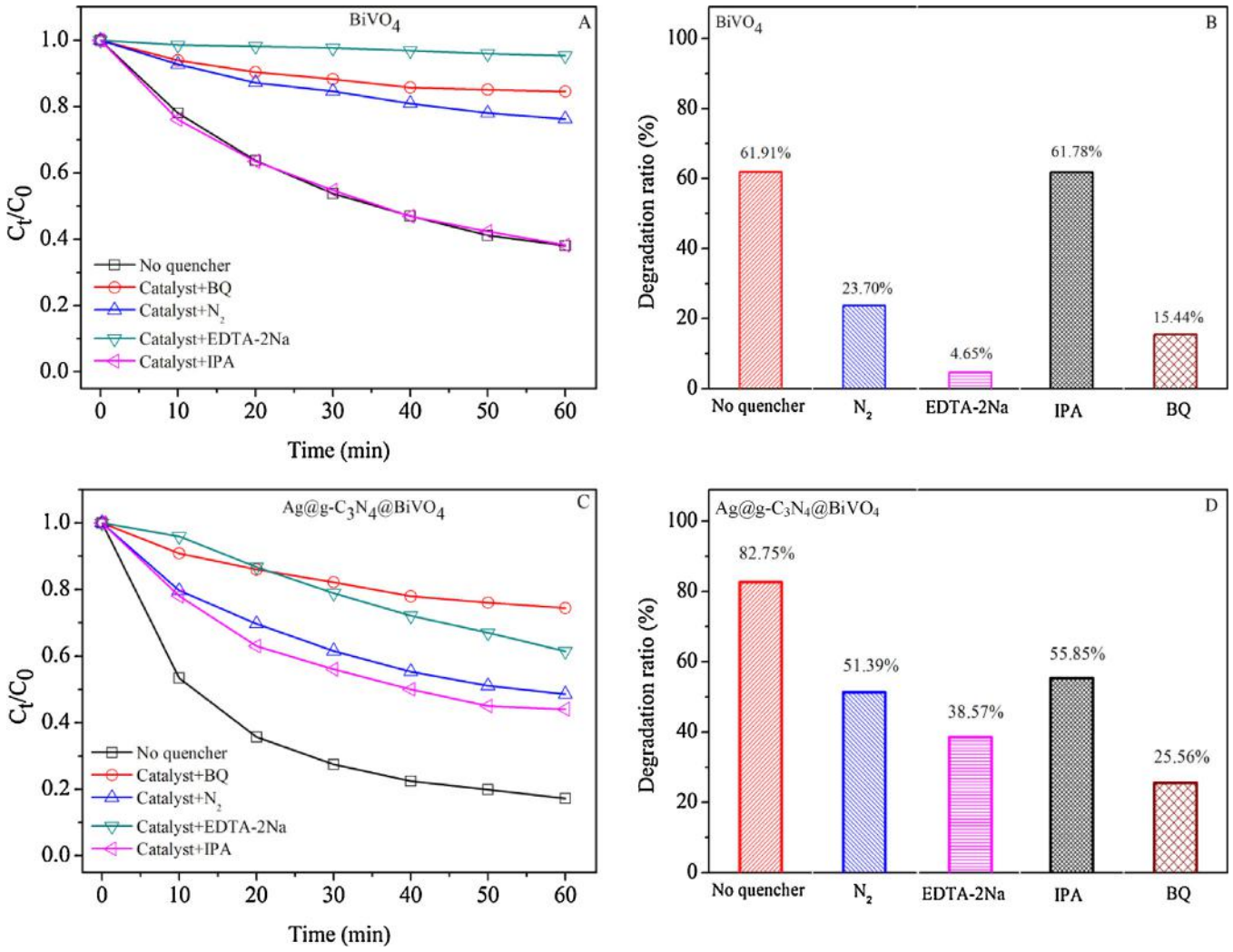

Fig. 12. Photoluminescence spectra of $BiVO_4$, g-C_3N_4, Ag@$BiVO_4$, g-C_3N_4@$BiVO_4$, Ag@g-C_3N_4@$BiVO_4$ samples.

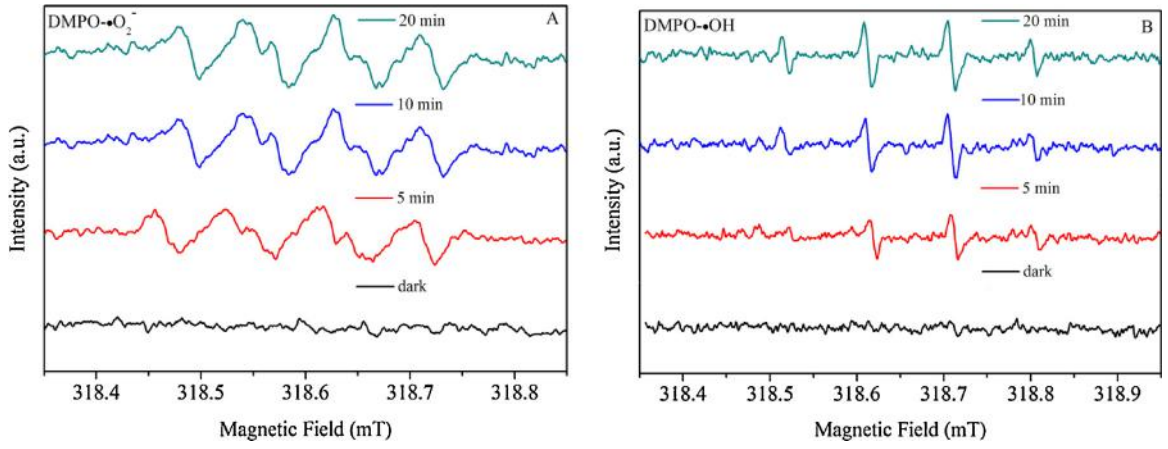

Fig. 13. The photocatalytic degradation plots of TC over $BiVO_4$ (A, B) and Ag@g-C_3N_4@$BiVO_4$ (C, D) with the addition of hole, $^{\bullet}O_2^-$ and •OH radical scavenger under visible light irradiation (λ > 420 nm).

diation (λ > 420 nm), the ESR spin-trap with DMPO technique was also performed on illuminated Ag@g-C_3N_4@$BiVO_4$ heterojunction. As indicated in Fig. 13A, there was no signal in the dark, while the light was on, the characteristic signals of DMPO-$^{\bullet}O_2^-$ could be observed, further confirming the forming of $^{\bullet}O_2^-$ during the photodegradation process. Additionally, the signal of •OH could be detected when exposed to the light (Fig. 13B). And the peaks intensity enhanced from the irradiation from 5 min to 20 min, suggesting •OH also played a vital role for the enhanced photocatalytic performance. Hence, the radicals trap experiments and ESR analysis revealed that the photocatalytic process was governed by the combined effect of $^{\bullet}O_2^-$, h^+ and •OH. The synergetic effect con-

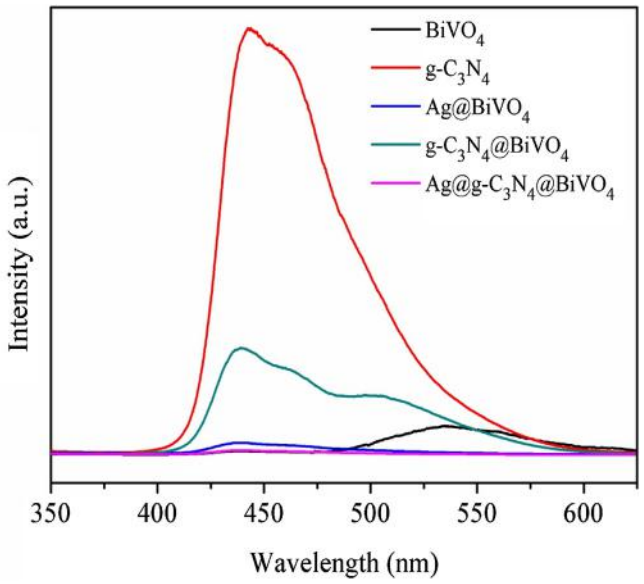

Fig. 14. ESR spectra of radical adducts trapped by DMPO in the Ag@g-C_3N_4@$BiVO_4$ dispersion under both the dark and visible light irradiation (λ > 420 nm) condition: (A) in methanol dispersion for DMPO-•O_2^-; (B) in aqueous dispersion for DMPO-•OH.

structed among Ag, g-C_3N_4 and $BiVO_4$ would lead to more active species generation, further to bring about the improvement of the photocatalytic activity towards TC degradation.

The photoluminescence spectrum has been verified to be an efficient approach to reflect the recombination efficiency of photogenerated electrons and holes through the present fluorescence intensity [48]. The stronger fluorescence intensity means that the photo-induced electrons and holes are prone to recombine and the lifetime of the photogenerated electrons are short. In return, if the photo-induced electrons could be prolonged, the intensities of the luminous peaks in the corresponding PL spectra will be very weak [49]. Fig. 14 shows the PL spectra of the single, binary and ternary photocatalysts. Compared with $BiVO_4$ and g-C_3N_4, modified $BiVO_4$ exhibited weaker luminous peak intensity. The corresponding signals of all the prepared catalysts could be listed as follows: Ag@g-C_3N_4@$BiVO_4$<Ag@$BiVO_4$<$BiVO_4$<g-C_3N_4@$BiVO_4$<g-C_3N_4, which was in good accordance with the results of photocatalytic activities. In particular, Ag nanoparticles and g-C_3N_4 co-modified $BiVO_4$ possessed the lowest intensity, indicating that the recombination rate of photo-induced electrons and holes of Ag@g-C_3N_4@$BiVO_4$ were effectively hindered. The SPR effect by Ag and heterojunction electric field formed between g-C_3N_4 and $BiVO_4$ should be the major reason for the inhabitation of the second recombination of electron-hole pairs. Additionally, to confirm the recombination inhabitation, analysis of charge carrier lifetime of pure $BiVO_4$ and Ag@g-C_3N_4@$BiVO_4$ were also provided. The decay curves for $BiVO_4$ (Fig. 15A) and Ag@g-C_3N_4@$BiVO_4$ (Fig. 15B) could be fitted well to a single and double-exponential function, respectively. The calculation lifetime of Ag@g-C_3N_4@$BiVO_4$ is 3.2340 ns, which is much longer than that of single $BiVO_4$ (i.e., 0.6018 ns). That was to say, the effective electron transport and charge separation efficiency were achieved, suggesting that synergistic effect among Ag, g-C_3N_4 and $BiVO_4$ was beneficial for photoactivity enhancement.

On the basis of the above-mentioned information, a more plausible explanation for the enhanced photocatalytic mechanism of Ag and g-C_3N_4 co-modified $BiVO_4$ ternary heterogeneous photocatalyst could be proposed and schematically described in Scheme 1. Given the calculation results above, the CB and VB edge potentials of $BiVO_4$ were at +0.46 eV and +2.86 eV, and the corresponding CB and VB edge potentials of g-C_3N_4 were at −1.23 eV and +1.51 eV, respectively. Under visible light irradiation, both $BiVO_4$ and g-C_3N_4 could easily produce photo-induced electron-hole pairs due to their narrow bandgaps. For g-C_3N_4@$BiVO_4$, the transport process of photogenerated carriers adhered to a typical heterojunction structure, which could be simplified as follows (Scheme 1A): the photogenerated electrons from the E_{CB} of g-C_3N_4 could transport to the E_{CB} of $BiVO_4$, and meanwhile the photoinduced holes from E_{VB} of $BiVO_4$ could transfer to the E_{VB} of g-C_3N_4. As a result, the separation and transfer process of charge carriers were significantly enhanced, and the carrier recombination processes were distinctly hampered, presented as a higher photocatalytic activity. For Ag@g-C_3N_4@$BiVO_4$ ternary heterojunction, the presence of metallic Ag could facilitate a Z-scheme transfer mechanism (Scheme 1B), because the general heterostructured mechanism couldn't interpret the forming •OH and the corresponding transfer of electrons and holes might be very slow [31,50]. Under visible light irradiation, on one hand, the CB potentials of $BiVO_4$ are more negative than that of metallic Ag due to its higher Schottky barriers at the metal-semiconductor interfaces. Thus the photogenerated electrons in the CB of $BiVO_4$ would shift to metallic Ag. On the other hand, the VB potentials of g-C_3N_4 are more positive than that of metallic Ag, so the photoinduced holes from g-C_3N_4 could also transform to metallic Ag. The electrons and holes could recombine in the Ag system, resulting in efficient electron-hole pairs separation. In such case, the photogenerated electrons in the E_{CB} of g-C_3N_4 could reduce the adsorbed O_2

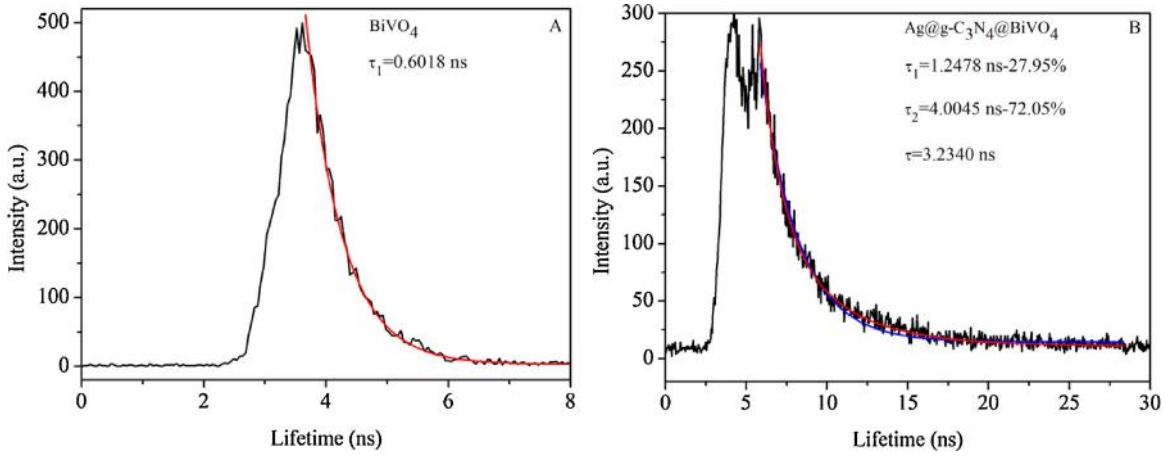

Fig. 15. Charge carrier lifetimes of the prepared $BiVO_4$ and Ag@g-C_3N_4@$BiVO_4$.

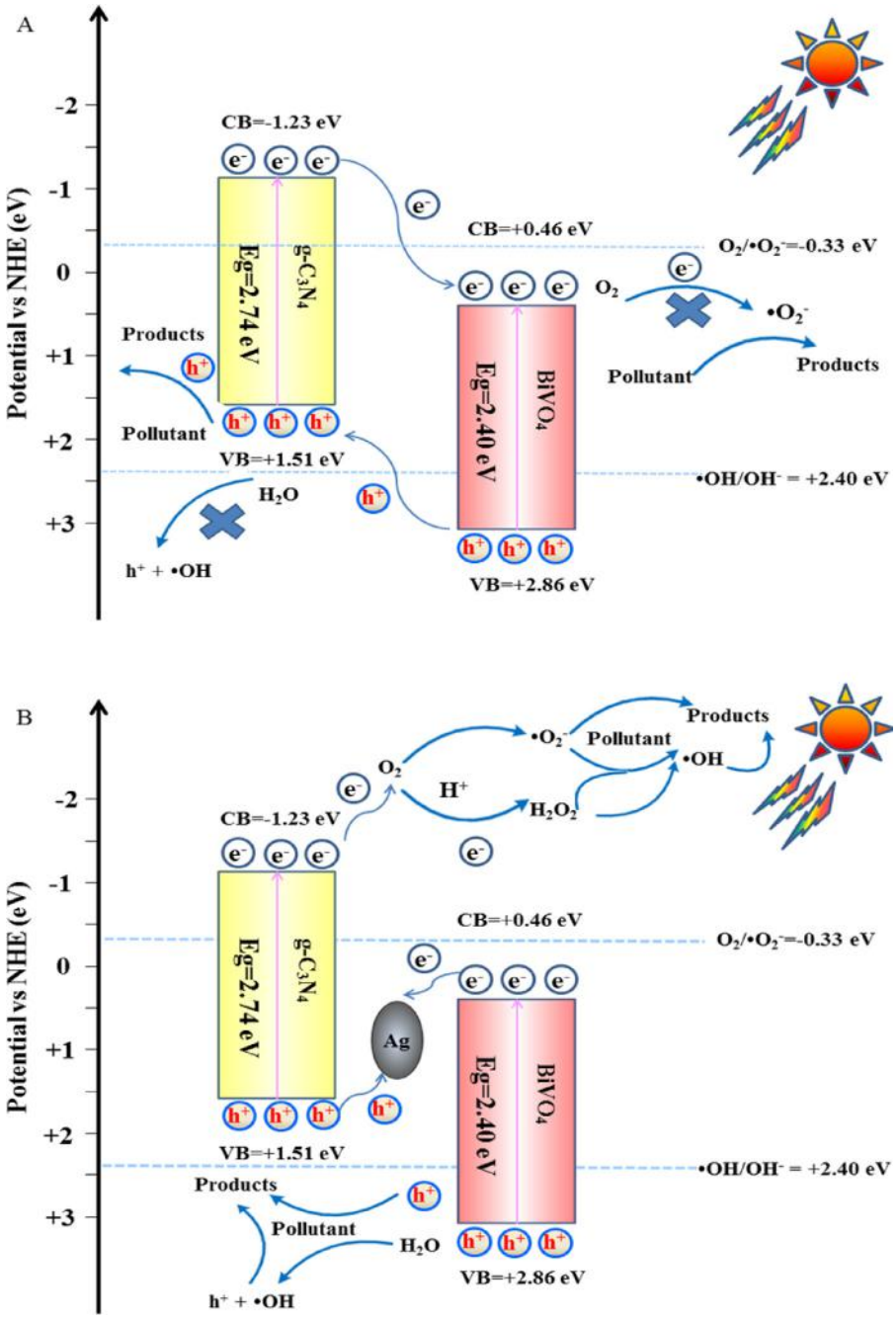

Scheme 1. Schematic diagram for the separation and transfer of photogenerated electron-hole pairs in g-C_3N_4@$BiVO_4$ binary (A) Ag@g-C_3N_4@$BiVO_4$ ternary (B) heterogeneous photocatalyst under visible light irradiation (λ > 420 nm).

to produce $^{\bullet}O_2^-$, because of the more negative position of E_{CB} of g-C_3N_4 than the $O_2/^{\bullet}O_2^-$ potential (ca. −0.33 eV [51]). Moreover, the adsorbed O_2 could also react with the water molecules and electrons to form H_2O_2. Subsequently, the generating H_2O_2 and $^{\bullet}O_2^-$ could be transformed into hydroxyl radicals (•OH). Concurrently, the photogenerated holes in the VB of $BiVO_4$ could combine with H_2O to form hydroxyl radicals (•OH), which could assigned to the fact that the position of E_{VB} of $BiVO_4$ is more positive than the $^{\bullet}OH/OH^-$ potential (ca. +2.40 eV [52]). The so-formed active species, h^+, $^{\bullet}O_2^-$ and •OH, could further effectively degrade the target pollutant (TC) into more small intermediates or directly into end products (CO_2 and H_2O). In summary, the metallic Ag played an important role as a transfer center in charge separation and the Z-scheme heterojunction could achieve higher enhancement in photo-induced electron-holes transferring and recombination ratio inhabitation, further to lead to superior photocatalytic performance.

4. Conclusions

In this study, a ternary heterojunction photocatalyst Ag@g-C_3N_4@$BiVO_4$ was successfully fabricated by anchoring Ag nanoparticles on the g-C_3N_4 and $BiVO_4$ with a wet-impregnation and photodeposition procedure. In comparison with single- and binary- component system, such as $BiVO_4$, g-C_3N_4, Ag@$BiVO_4$, g-C_3N_4@$BiVO_4$, the ternary Ag@g-C_3N_4@$BiVO_4$ composite possessed the distinctly enhanced photocatalytic activity towards TC degradation under solar light, visible light, even near infrared light

irradiation. The coexisting Fe^{3+} would be in favorable for the photoactivity enhancement because it could adsorb the light to produce active species, •OH under weakly acidic solution and capture photo-induced electrons and holes, to promote charge carriers separation. The presence of NO_3^- and Ca^{2+} played a negative role in the degradation process, which could be ascribed to the increasing electrostatic repulsion and the forming metal complexes, respectively. The introduction of metallic Ag acted as a charge transfer center, the electrons from the CB of $BiVO_4$ and holes from the VB of g-C_3N_4 would recombine in this site. The synergistic effects could be concluded as the following aspects: (i) effective photo-generated electron-hole pairs separation, (ii) slower charge recombination rate and (iii) the extension of visible light response range. The active species $•O_2^-$, h^+ and •OH were produced in the forming Z-scheme system. The present study may provide a new approach to construct novel and highly efficient ternary heterostructured photocatalysts and facilitate their practical applications for environmental remediation.

Acknowledgments

This research was financially supported by the project of National Natural Science Foundation of China (NSFC) (Nos. 51378188, 51478170, 51508178), Doctoral Fund of Ministry of Education of China (20130161120021).

References

[1] X.B. Chen, L. Liu, P.Y. Yu, S.S. Mao, Science 221 (2011) 746–750.
[2] A. Hameed, M. Aslam, I.M.I. Ismail, N. Salah, Appl. Catal. B: Environ. 163 (2015) 444–451.
[3] R. Marschall, Adv. Funct. Mater. 24 (17) (2014) 2421–2440.
[4] E.S. Kim, N. Nishimura, G. Magesh, J.Y. Kim, J. Am. Chem. Soc. 135 (2013) 5375–5383.
[5] S.J.A. Moniz, S.A. Shevlin, D.J. Martin, Z.X. Guo, Energy Environ. Sci. 8 (2015) 731–759.
[6] J. Luo, X. Zhang, J. Zhang, ACS Catal. 5 (2015) 2250–2254.
[7] Z. Wang, K. Teramura, S. Hosokawa, T. Tanaka, Appl. Catal. B: Environ. 163 (2015) 241–247.
[8] H. Lin, L. Li, M. Zhao, X. Huang, X. Chen, G. Li, J. Am. Chem. Soc. 134 (2012) 8328–8331.
[9] X. Zhang, H. Li, S. Wang, F.R.F. Fan, A.J. Bard, J. Phys. Chem. C 118 (2014) 16842–16850.
[10] J.X. Wang, P.X. Wang, Y.T. Cao, J. Chen, Appl. Catal. B: Environ. 136–137 (2013) 94–102.
[11] Z.Y. Zhang, D.L. Jiang, D. Li, M.Q. He, M. Chen, Appl. Catal. B: Environ. 183 (2016) 113–123.
[12] L. Sun, X. Zhao, C.J. Jia, Y. Zhou, X. Cheng, J. Mater. Chem. 22 (2012) 23428–23438.
[13] X. Wang, S. Li, Y. Ma, H. Yu, J. Yu, J. Phys. Chem. C 115 (2011) 14648–14655.
[14] J.G. Li, J.X. Yu, Y.P. Low, J. Fang, X.B. Xiao, J. Mater. Chem. A 3 (2015) 2485–2534.
[15] S. Bai, J. Jiang, Q. Zhang, Y.J. Xiong, Chem. Soc. Rev. 44 (2015) 2893–2939.
[16] N.C. Castillo, A. Heel, T. Graule, C. Pulgarin, Appl. Catal. B: Environ. 95 (2010) 335–347.
[17] H.W. Huang, Y. He, X. Du, P.K. Chu, ACS Sustain. Chem. Eng. 3 (12) (2015) 3262–3273.
[18] Z.J. Zhou, M.C. Long, W.M. Cai, J. Cai, J. Mol. Catal. A: Chem. 353–354 (2012) 22–28.
[19] X.X. Chang, T. Wang, P. Zhang, J.J. Zhang, A. Li, J. Am. Chem. Soc. 137 (2015) 8356–8359.
[20] C.J. Li, S.P. Wang, T. Wang, Y.J. Wei, P. Zhang, J.L. Gong, Small 14 (2014) 2783–2790.
[21] Q. Yuan, L. Chen, M. Xiong, J. He, S.L. Luo, C.T. Au, Chem. Eng. J. 255 (2014) 394–402.
[22] H. Li, K. Yu, X. Lei, J. Phys. Chem. C 119 (39) (2015) 22681–22689.
[23] N. Wetchakun, S. Chaiwichain, J. Chen, ACS Appl. Mater. Interfaces 4 (2012) 3718–3723.
[24] Q. Yang, F. Chen, X.M. Li, D.B. Wang, Y. Zhong, G.M. Zeng, RSC Adv. 6 (2016) 60291–60307.
[25] Y. Ji, J. Cao, L. Jiang, Y. Zhang, Z. Yi, J. Alloys Compd. 590 (2014) 9–14.
[26] M. Ou, Q. Zhong, S. Zhang, L. Yu, J. Alloys Compd. 626 (2015) 401–409.
[27] L.Q. Shao, D.L. Jiang, P. Xiao, L.M. Zhu, Appl. Catal. B: Environ. 198 (2016) 200–210.
[28] X. Xin, J.Y. Lang, T.T. Wang, Y.G. Su, Y.X. Zhao, Appl. Catal. B: Environ. 181 (2016) 197–209.
[29] C. Hu, T.W. Peng, X.X. Hu, Y.L. Nie, X.F. Zhou, J. Am. Chem. Soc. 132 (2010) 857–862, 9 857.
[30] M.O. Ansari, M.M. Khan, S.A. Ansari, ACS Appl. Mater. Interfaces 6 (2014) 8124–8133.
[31] X.P. Xiao, J.H. Wei, Y. Yang, R. Xiong, ACS Sustain. Chem. Eng. 4 (2016) 3017–3023.
[32] Y.F. Chen, W.X. Huang, D.L.A.C.S. Appl, Mater. Interfaces 6 (2014) 14405–14414.
[33] Y.J. Wang, Y.N. Zhang, Z.Q. Jiang, G.Y. Jiang, Appl. Catal. B: Environ. 185 (2016) 307–314.
[34] F. Chen, Q. Yang, Y. Zhong, H.X. An, J.W. Zhao, T. Xie, Water Res. 101 (2016) 555–563.
[35] F. Chen, Q. Yang, X.M. Li, G.M. Zeng, Appl. Catal. B: Environ. 200 (2017) 330–342.
[36] Y.D. Deng, L. Tang, G.M. Zeng, J.J. Wang, J. Mol. Catal. A: Chem. 421 (2016) 209–221.
[37] F. Chen, Q. Yang, C.G. Niu, X.M. Li, C. Zhang, Catal. Commun. 73 (2016) 1–6.
[38] H. Wang, X.Z. Yuan, Y. Wu, G.M. Zeng, Appl. Catal. B: Environ. 174 (2015) 445–454.
[39] B. Zhou, X. Zhao, H.J. Liu, J.H. Qu, C.P. Huang, Appl. Catal. B: Environ. 99 (2010) 214–221.
[40] Y. Chen, K. Liu, Chem. Eng. J. 302 (2016) 682–696.
[41] F. Wu, N.S. Deng, Chemosphere 41 (8) (2000) 1137–1147.
[42] Y.M. Wu, J.L. Zhang, L. Xiao, F. Chen, Appl. Catal. B: Environ. 88 (2009) 525–532.
[43] L. Jin, X. Amaya-Mazo, M.E. Apel, S.S. Sankisa, A. Han, Biophys. Chem. 128 (2007) 185–196.
[44] H.G. Yu, L.L. Xu, P. Wang, X.F. Wang, J.G. Yu, Appl. Catal. B: Environ. 144 (2014) 75–82.
[45] Y.K. Li, S.Y. Dong, Y.F. Wang, J.Y. Sun, Y.F. Li, J. Mol. Catal. A: Chem. 387 (2014) 138–146.
[46] H. Wang, X.Z. Yuan, H. Wang, X.H. Chen, Z.B. Wu, Appl. Catal. B Environ. 193 (2016) 36–46.
[47] F. Chen, Q. Yang, C.G. Niu, X.M. Li, C. Zhang, RSC Adv. 5 (2015) 63152–63164.
[48] Y.C. Huang, W.J. Fan, B. Long, H.B. Li, F.Y. Zhao, Appl. Catal. B: Environ. 185 (2016) 68–76.
[49] Y.Y. Bu, Z.Y. Chen, C.J. Sun, Appl. Catal. B: Environ. 179 (2015) 363–371.
[50] Y.M. He, L.H. Zhang, B.T. Teng, M.H. Fan, Environ. Sci. Technol. 49 (2015) 649–656.
[51] X.L. Fu, W.M. Tang, L. Ji, Chem. Eng. J. 180 (2012) 170–177.
[52] S. Meng, X. Ning, T. Zhang, S.F. Chen, Phys. Chem. Chem. Phys. 17 (2015) 11577–11585.